

ShapeICP: Iterative Category-level Object Pose and Shape Estimation from Depth

Yihao Zhang¹ and John J. Leonard¹

Abstract—Category-level object pose and shape estimation from a single depth image has recently drawn research attention due to its wide applications in robotics and self-driving. The task is particularly challenging because the three unknowns, object pose, object shape, and model-to-measurement correspondences, are compounded together but only a single view of depth measurements is provided. The vast majority of the prior work heavily relies on data-driven approaches to obtain solutions to at least one of the unknowns and typically two, running with the risk of failing to generalize to unseen domains. The shape representations used in the prior work also mainly focus on point cloud and signed distance field (SDF). In stark contrast to the prior work, we approach the problem using an iterative estimation method that does not require learning from any pose-annotated data. In addition, we adopt a novel mesh-based object active shape model that has not been explored by the previous literature. Our algorithm, named ShapeICP, has its foundation in the iterative closest point (ICP) algorithm but is equipped with additional features for the category-level pose and shape estimation task. The results show that even without using any pose-annotated data, ShapeICP surpasses many data-driven approaches that rely on the pose data for training, opening up new solution space for researchers to consider.

I. INTRODUCTION

We investigate the task of estimating the pose and shape of an object given a single depth image of it. The object instance is only known up to its semantic category. Its exact geometry (i.e. CAD model) is unavailable to us. Such a problem is commonly encountered in many scenarios ranging from self-driving to home robots. For example, self-driving may require estimation of the poses and shapes of other vehicles on the street without knowing the detailed CAD models of them apriori. Similarly, home robots may require estimation of the poses and shapes of table top objects in order to manipulate them. Because of the wide applications and the significance of this task, it has drawn substantial research attention in recent years.

The category-level object pose and shape estimation problem is typically set up such that the instance segmentation and semantic classification of the object is done on the accompanied RGB image with an off-the-shelf method [1]–[20]. However, even after factoring out the object detection and segmentation problem, inferring the object pose and shape from the segmented depth image remains challenging due to the three entangled unknowns, object pose, object shape and model-to-measurement correspondences. It requires us to know two of the three unknowns to reduce

the problem to an easily solvable one. Specifically, if we know the object shape and how the measurements correspond to the points on the surface of the shape, it is reduced to the problem of aligning two point sets which the Umeyama algorithm [21] can solve. If the object pose and the correspondences between the measurements and a category-level shape template are known, one can transform the template to the same pose as the measurements and translate the template points onto the corresponding measurements to obtain the shape. Researchers often recognize the correspondences as an unknown and deform the template to fit the measurements [22]–[25] using Chamfer loss where the closest points are the correspondences [22]–[24], [26], [27]. However, with the three variables all left unknown, the problem is extremely difficult.

Most prior methods exploit neural networks to learn a mapping from inputs such as the RGB image, the depth image, and the categorical shape prior, to one or two of the three unknowns. For example, in [1], a deformation field is learned to deform the shape prior to obtain the object shape and a correspondence matrix is predicted to draw correspondences between the model shape and the back-projected depth points for pose estimation with Umeyama [21]. Although these learning methods greatly factor away the complexities in the problem by leveraging data and have achieved excellent performance on benchmarks, they are faced with potential failures caused by any domain change and tedious data curation process for training when they are deployed to a new environment. In the object pose and shape estimation task, the ground truth pose of an object is especially painstaking to annotate since so far there has been no scalable and easily accessible approach to measure the pose of an object. On the other hand, virtually all the prior methods focus on either point cloud or signed distance field (SDF) as the shape representation. Point clouds are flexible but they do not have the notion of surface, while SDF entails unfavorable computational complexity which is often scaled cubically with the resolution.

In this work, we take a radically different approach. First, in contrast to prior methods, we adopt a novel mesh-based active shape model (ASM) [28] as the object shape representation. Meshes incorporate the notion of surface, being superior to point clouds. They are also inherently a geometric representation, unlike SDF or occupancy grid where the geometry is represented implicitly and some processes such as finding the zero level set (SDF) or marching cubes [29] (occupancy grid) are required to extract the geometry. The use of meshes in category-level object pose

¹Yihao Zhang and John Leonard are with the Computer Science and Artificial Intelligence Laboratory, Massachusetts Institute of Technology, Cambridge, MA 02139 USA {yihaozh, jleonard}@mit.edu

and shape estimation is also a relatively untapped terrain in the literature. It is worth being explored more. Second, we devise an iterative estimation algorithm based on the iterative closest point (ICP) algorithm [30] and many other classical estimation techniques without training any module on the pose-annotated data. The method has an option to use an image-based shape classification network for shape initialization to boost the estimation performance. We consider that in practice object ground-truth shape is more accessible than its ground-truth pose since object scanning and depth fusion techniques [31] are mature.

We evaluate our method on the NOCS REAL dataset [32] and find better or comparable performance to many learning-based methods even though our method is at the disadvantage that no pose-annotated data are used. Besides the performance comparison, the evaluation of our method also reveals what can be already accomplished without learning and why learning may be needed at some places in this estimation task. These insights are traditionally difficult to draw from the evaluation of black-box style learning-based methods.

II. RELATED WORK

We will review the related work in terms of which of the three unknowns, object pose, object shape, and model-to-measurement correspondences are predicted by neural networks. We will also discuss shape representations used in the literature.

A. Category-Level Pose and Shape Estimation

Predicting shape and correspondences. One of the most popular approaches is predicting the object shape as well as the correspondences between the shape and the measured depth points. The seminal work NOCS [32] belongs to this category. The predicted NOCS map encodes the depth profile (i.e. shape) of the observed object in its canonical pose. The NOCS map also corresponds pixel-to-pixel to the measured depth image, being essentially a combined prediction of the object shape and the correspondences. The Umeyama algorithm [21] can solve the transformation between the NOCS map and the depth image. Another work is [18] where the authors first use Mesh R-CNN [26] to predict a metric-scale mesh of the object shape from the image and then predict the NOCS map to solve for the pose. Among the methods that predict both shape and correspondences, a notable line of work [1]–[6] attempts to predict the deformation applied to a categorical shape prior to obtain the object shape and a correspondence matrix to associate the model (i.e. the deformed prior) points to the measured depth points. The Umeyama algorithm [21] is then engaged to solve the transformation. One representative work is Shape Prior [1] where a network takes in the RGB image patch, back-projected depth points, and the categorical shape prior to predict the deformation field and the correspondence matrix.

Predicting shape and pose. A more straightforward approach is predicting the pose and shape directly. Methods in this category often have an iterative closest point (ICP) [30]

post-processing step to refine the predicted pose. One highly recognized work is CASS [7]. It incorporates a variational auto-encoder (VAE) [33] to learn a point cloud based shape embedding space. During inference, the shape latent code is predicted given the RGB-D image patch. The predicted latent code is both decoded to the shape in its canonical pose and fed to the module for pose prediction. There are various other solutions in this category of methods. For example, CenterSnap [34] and ShAPO [35] forgo the use of the region of interest (RoI) based Mask R-CNN [36] for object detection. Instead they build a YOLO-style [37] one-shot estimation pipeline. The object poses and shape codes along with the object detection are predicted in one shot on a heat map. iCaps [9] selects the rotation by comparing the depth image features to the features in a pre-computed code book and predicts the DeepSDF [38] latent vector as the shape representation. SDFest [8] refines the predicted pose and shape by comparing the rendered depth image to the actual depth image. Other methods that directly regress shape and pose to various extent include [10]–[12], [39].

Predicting pose. Another set of methods bypasses the shape estimation and only estimates the pose. FS-Net [40] extracts rotation-aware features through a scale and shift-invariant 3D graph convolution network. It also decouples the rotation into two perpendicular vectors for prediction. SAR-Net [13] transforms a categorical template to the same rotation as the observed point cloud by neural networks. The transformed template is aligned with the original template by Umeyama [21] to find the rotation. The translation and size are predicted based on a mirroring-completed point cloud which is the measured point cloud concatenated with the mirrored version of the point cloud with respect to the plane of symmetry. Both the template transforming step and mirroring-completion step are performed by neural networks which have to implicitly learn the object pose prediction task since both the transformation and the plane of symmetry are pose dependent. MH6D [14] transforms the measured point cloud randomly three times, regresses poses for the three point clouds and enforces consistency among the regressed results.

Predicting correspondences. Several methods use key-point or descriptor matching as the base to solve the problem. [41] assumes known model-to-measurement correspondences provided by neural keypoint matching and solves an alignment problem between the model keypoints and the measurement keypoints. Instead of only estimating the SIM(3) pose as in Umeyama [21], the method additionally estimates the parameters for an active shape model (ASM) [28] of the object. Fortunately, the ASM is linear and can be treated similarly as the translation. The method also features a graph-theoretic approach and an outlier-robust solver to handle false correspondences. [42] is an earlier work that essentially shares the same problem formulation as [41] but with a different solver that does not consider the outlier issue. [15] computes semantic primitives using a part segmentation network. It derives a SIM(3)-invariant shape descriptor from the primitives and minimizes the discrepancy between the

observed descriptor and the model descriptor to optimize the shape. Once the shape is optimized, Umeyama [21] is performed on the primitive centers and the measured point cloud to estimate the pose.

Optimization-based. A few methods resort to optimization for the pose and shape estimation avoiding direct regression. Neural Analysis-by-Synthesis [16] leverages neural rendering to render an image from the object shape code and pose. The rendered image is compared against the actual image for the shape code and pose optimization. It starts from multiple initial states in parallel to avoid local minima. DirectShape [17] sets up the optimization losses by silhouette matching and left-right stereo photo consistency using an ASM of a signed distance field (SDF) representation for the shape. As the work is for vehicle estimation only, it engages strong regularization such as the ground plane constraint to alleviate the optimization difficulty. TransPoser [19] directly outputs a rendered depth image using a neural network given the object pose and shape code to compare with the actual depth image. As the method is applied on RGB-D image sequences, it sequentially updates the pose and shape code with a Transformer [43]. ELLIPSDF [20] employs a bi-level shape representation which returns two levels of shape, an SDF and an ellipsoid, from the latent code. It estimates an initial pose by fitting the ellipsoid to the object segmentation. The optimization of the pose and shape is performed to minimize the signed distance of the measured depth points computed from both the SDF representation and the ellipsoid representation.

As we have seen, previous methods commonly adopt data-driven solutions. Pose-annotated data are exploited in almost all the prior work either explicitly or implicitly. Even the optimization-based methods may actually require extra information such as an RGB-D sequence instead of a single image [19], [20] or application-specific constraints [17]. Our method works completely without pose-annotated data. The addition of an optional shape classification network merely requires shape-annotated data, which also falls into the rare category of predicting only the shape, a direction not well explored by the prior work.

B. Shape Representation

The active shape model (ASM) [28] has been employed in the category-level object pose and shape estimation task [10], [17], [41] and also the 3D object shape reconstruction task [44], [45]. The ASM has the advantage of being a simple linear model which is more efficient to back-propagate through during optimization compared to a neural network. The object ASM is typically point-based [10], [41], [42] or SDF-based [17], [44], [45]. In this work, we explore a mesh-based ASM. Methods in the literature for category-level object pose and shape estimation primarily use SDF and point cloud as the shape representation, it is interesting to explore more in the mesh representation.

III. METHOD

A. Overview

Our task is to estimate the SIM(3) pose and shape of an object which is only known up to its semantic category given a single depth image of it. We assume that instance segmentation of the object and its class label are provided by an off-the-shelf method such as Mask RCNN [36] as typically used in the prior work [1]–[17]. In order to estimate the shape, the shape representation of the object has to be malleable to the shapes within the category. We hence adopt a mesh-based object active shape model (ASM) [28] for its flexibility and surface representability. In order to have consistent number of vertices and vertex connectivity across all the object models in the database for Principal Component Analysis (PCA) which is required to build the ASM, we deform a spherical template mesh to wrap around each object model and run PCA on the deformed templates. After obtaining the ASM offline, we estimate the pose and shape by transforming and fitting the shape model to the observed depth points. The optimization is achieved by an augmented iterative closest point (ICP) algorithm which in addition to the existing pose estimation step has a shape deformation step for shape estimation. We thus name our algorithm ShapeICP. However, ICP is a local solver and so is the base form of ShapeICP. This becomes a significant challenge due to the lack of an initial guess. To overcome it, ShapeICP is outfitted with multi-hypothesis tracking for rotation estimation, expectation maximization (EM) for robust correspondence handling, and shape classification for shape initialization. The multi-hypothesis estimation is paramount to the success of the algorithm. It has hypothesis scoring functions based on closest point distance, symmetry, and rendering. The full pseudo-algorithm of ShapeICP can be found in Alg. 1.

B. Mesh-based Object Active Shape Model

Template deformation. Mesh-based ASMs have been applied to human faces [46], [47] but not yet in the task of object pose and shape estimation. The bottleneck is that object models from a database such as ShapeNet [48] have different numbers of vertices and different vertex connectivity even within the same category (see Fig. 1), making it difficult to draw corresponding vertices across models for PCA. To solve this challenge, we deform a template mesh to wrap around each object model and run PCA on the vertices of the deformed templates for all the object models within a category. More specifically, we denote a mesh by $\mathcal{M} = (\mathcal{V}, \mathcal{E}, \mathcal{F})$, where $\mathcal{V} = \{v_i\}_{i=1}^V$ are the V vertices in the mesh, $\mathcal{E} = \{e_i\}_{i=1}^E$ is the set of E tuples that each store the indices of a pair of vertices connected by an edge, $\mathcal{F} = \{f_i\}_{i=1}^F$ is the set of F tuples of indices of vertices on the same faces. To deform the template mesh \mathcal{M}_s to a target mesh \mathcal{M}_t , we first randomly sample points on the mesh surfaces with N points from the template mesh $p_n \sim \mathcal{M}_s$ and M points from the target mesh $q_m \sim \mathcal{M}_t$ (here $N = M$). The deformation is done by minimizing the

similar losses as in [26], [27], [49]:

$$\mathcal{L}_c = \frac{1}{N} \sum_n \min_m \|p_n - q_m\|_2^2 + \frac{1}{M} \sum_m \min_n \|p_n - q_m\|_2^2 \quad (1)$$

which is the Chamfer distance between the two sets of sampled points. To regularize the template mesh during the deformation process, a normal consistency loss is imposed on the template mesh:

$$\mathcal{L}_n = \frac{1}{E} \sum_e 1 - \cos(\mathbf{n}_{f_{e+}}, \mathbf{n}_{f_{e-}}) \quad (2)$$

where $\mathbf{n}_{f_{e+}}$ and $\mathbf{n}_{f_{e-}}$ are the normals of the two faces that share edge e , and \cos is the cosine distance. This loss regularizes the surface normals to be smooth. To avoid overly long outlier edges in the template mesh, an edge length loss is added:

$$\mathcal{L}_e = \frac{1}{E} \sum_e \|v_{e+} - v_{e-}\|_2^2 \quad (3)$$

where v_{e+} and v_{e-} are the vertices connected by the edge e . A Laplacian smoothing loss is also enforced on the template mesh to encourage the vertices to move along with their neighbors and potentially avoid mesh self-intersection:

$$\mathcal{L}_l = \frac{1}{V} \sum_i \|v_i - \frac{1}{|\mathcal{N}(i)|} \sum_{j \in \mathcal{N}(i)} v_j\|_2 \quad (4)$$

where $\mathcal{N}(i) = \{j\} \forall (i, j) \in \mathcal{E}$ is the set of neighboring vertices of vertex v_i . The overall objective function is $\min_{\mathcal{V}_s} \mathcal{L}_c + \lambda_n \mathcal{L}_n + \lambda_e \mathcal{L}_e + \lambda_l \mathcal{L}_l$, where λ 's are the weights for the loss terms. This optimization is carried out by stochastic gradient descent (SGD) [50] starting from a spherical template mesh. We remark that category-specific templates can be used to better fit the topology of each class but we choose a spherical template for its generality. An example of the deformation process is visualized in Fig. 2.

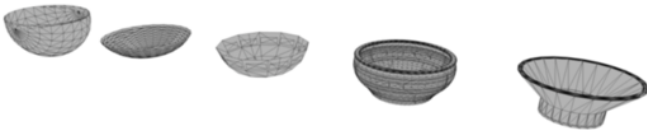


Fig. 1: A few example objects in the same category but with different numbers of vertices and different vertex connectivity.

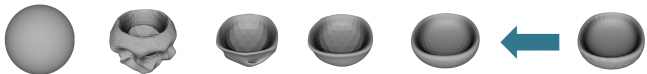


Fig. 2: An example of the template deformation process with the initial template on the left and the target mesh on the right side of the arrow.

PCA. Now that we have acquired a set of deformed templates that take on the model shapes across a category and have consistent number of vertices and connectivity, we can build a feature vector for each model by concatenating the vertices of its deformed template, i.e. $[v_1 \dots v_{V_s}]$, and then

run PCA on all the feature vectors to obtain our category-level mesh-based ASM. A vertex in the final ASM with K principal components is expressed as

$$v_i = b_{0,i} + \sum_{k=1}^K c_k b_{k,i} \quad (5)$$

where $b_{0,i}$ is the vertex in the mean shape corresponding to v_i , $b_{k,i}$ is the corresponding vertex in basis k , and $\{c_k\}_{k=1}^K$ are the weights for the bases. These weights parameterize the shape. Fig. 3 visualizes the vertices of the bases and the final shape in an example ASM. The edges and faces of the mesh-based ASM are inherited from the template mesh.

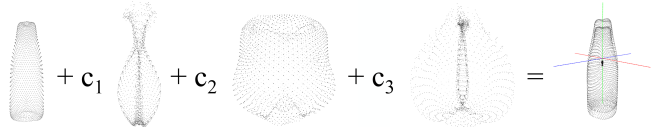


Fig. 3: Visualization of the vertices of the bases and the final shape in an example ASM. The final shape on the right shows how the mean shape is displaced by the weighted bases (the scale of the bases is much smaller than the mean so the bases are enlarged for clarity.)

C. Alternating Pose and Shape Optimization

Formulation. To introduce our ShapeICP formulation, we need sample points on the ASM. Each sampled point can be expressed as

$$p_n = \sum_{i \in F(n)} \mu_{n,i} v_i \quad \text{s.t.} \quad \sum_{i \in F(n)} \mu_{n,i} = 1 \quad (6)$$

where $F(n)$ is a function that maps the sample index n to a randomly selected face, and $\mu_{n,i}$ are randomly generated interpolation weights for this sample. These interpolation weights are fixed during the optimization. Combining with (5), $p_n = \sum_{i \in F(n)} \mu_{n,i} (b_{0,i} + \sum_{k=1}^K c_k b_{k,i})$. We now introduce the ShapeICP formulation:

$$\min_{\substack{R \in \text{SO}(3), t \in \mathbb{R}^3, s \in \mathbb{R}_{++} \\ \mathbf{c} = [c_1 \dots c_K] \in \mathbb{R}^K}} \frac{1}{M} \sum_{m=1}^M \min_n \|sRp_n + t - q_m\|_2^2 \quad (7)$$

where $\{q_m\}_{m=1}^M$ (overloaded notation) are now the object depth points segmented from the depth image and back-projected to 3D using the camera intrinsics, R , t , and s are the object rotation, translation, and scale to be estimated, \mathbf{c} which enters the objective function through p_n is the ASM shape code also to be estimated. For each measurement q_m , (7) encourages the transformed model points to be close to the measurements, which is similar to the ICP objective function [30] but with the addition of the shape parameter \mathbf{c} . We also remark that formulation (7) equivalently works for a point-based ASM where p_n is simply a point in the ASM point cloud. However, mesh-based ASM has the notion of surface and thus is a better geometric representation. Furthermore, a mesh model enables the possibility of rendering to be used in Section III-D.

Core algorithm. We make two observations of (7). First, if the shape code \mathbf{c} is given, the problem shares the same

objective function with ICP. Second, if the SIM(3) pose is given, the problem mimics the mesh deformation problem introduced in Section III-B except that (7) is only one-sided Chamfer distance and the optimization variable is the shape code instead of the vertices. These two observations lead to an intuitive alternating minimization algorithm to solve (7):

- *Pose step:* Associate each measurement q_m to the closest transformed model point $\hat{s}\hat{R}p_n + \hat{t}$ (i.e. solving \min_n in (7)) using the last estimates \hat{c} , \hat{R} , \hat{t} , and \hat{s} . Solve for the incremental R , t , and s with Umeyama [21] to further align the model points with the measurements while keeping c fixed.
- *Shape step:* Re-associate each q_m to the closest model point using the updated \hat{R} , \hat{t} , and \hat{s} . Solve for c as if it is a mesh deformation problem while keeping R , t , and s fixed.

After the pose step, the incremental R , t , and s are accumulated onto the estimates \hat{R} , \hat{t} , and \hat{s} .

Shape step. In the shape step, we include the regularization losses (2) – (4). The final objective function \mathcal{L}_{sc} (*sc*: shape code) in the shape step is $\min_c \mathcal{L}_{sc} = \min_c \mathcal{L}_{ps} + \lambda_n \mathcal{L}_n + \lambda_e \mathcal{L}_e + \lambda_l \mathcal{L}_l$, where \mathcal{L}_{ps} (*ps*: pose shape) refers to the objective function in (7) and λ 's are the weights. These weights can be reused from Section III-B if we center and normalize the observed point cloud, and shift and normalize the transformed model points by the same amount (because the ShapeNet [48] objects in Section III-B are all centered and normalized).

Since this is an iterative coordinate-descent style algorithm, at each iteration the shape step does not have to solve to the optimum. Only a few steps of gradient descent is performed on c starting from the last estimate \hat{c} . We also stop running the shape step in the last few iterations for better empirical performance.

D. Coping with Local Minima

Category-level object pose and shape estimation given only a single-view depth image naturally comes with large ambiguity (Fig. 4) since many configurations of the variables may fit equally well to the observed partial object point cloud. In other words, the optimization landscape exhibits many local minima, which hurt the performance of a local solver such as ShapeICP. In this section, we develop several strategies to cope with the local minima.

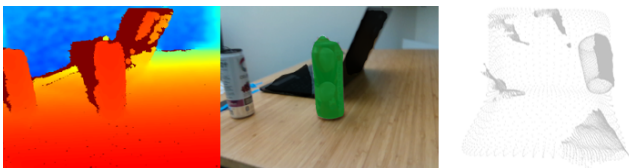


Fig. 4: An occluded depth observation of the laptop (whose point cloud is fragmented in the right picture) causes ambiguity. The fit model (whose vertices are visualized as the organized point set) has pose error and collides with another object.

Expectation maximization (EM). The correspondences between the measured depth points and the model points

can be treated as latent variables. Instead of hard one-to-one associations, EM allows softer associations [51], reducing the chance of being stuck at a local minimum. We integrate EM into our ShapeICP formulation following a similar approach as in [52]. Each measurement m is now accompanied by a latent variable z_m that models the association of this measurement. Specifically,

$$\mathcal{P}(z_m = n) = \begin{cases} \frac{1}{Q} & \text{if } n \in \mathcal{N}_Q(q_m) \\ 0 & \text{otherwise} \end{cases} \quad (8)$$

where $\mathcal{P}(z_m = n)$ is the probability of q_m associated to p_n and $\mathcal{N}_Q(q_m)$ finds the Q closest transformed model points to q_m (i.e. the top Q solutions to $\arg \min_n \|sRp_n + t - q_m\|_2^2$). We further model the conditional data likelihood as

$$\mathcal{P}(q_m | z_m = n) = \mathcal{N}(sRp_n + t - q_m; 0, \Sigma_m) \quad (9)$$

where $\mathcal{N}(\cdot; 0, \Sigma_m)$ is a zero-mean Gaussian distribution with covariance Σ_m (i.e. conditioned on q_m associated to p_n , the residual follows a Gaussian distribution). Assuming independence $q_m | z_m \perp z_{m'}$, $q_m | z_m \perp q_{m'} | z_{m'}$ and $z_m \perp z_{m'}$, and isotropic covariance $\Sigma_m = \text{diag}(\sigma_m^2)$, the objective function \mathcal{L}_{em} derived from EM is (explanations about the probabilistic models and the independence assumptions, and the derivation of EM can be found in the appendix):

$$\min_{\substack{R \in \text{SO}(3), t \in \mathbb{R}^3, s \in \mathbb{R}^{++} \\ c = [c_1 \dots c_K] \in \mathbb{R}^K}} \sum_{m=1}^M \sum_{n \in \mathcal{N}_Q(q_m)} w_{mn} \|sRp_n + t - q_m\|_2^2 \quad (10)$$

where

$$w_{mn} = \frac{\mathcal{N}(\hat{s}\hat{R}\hat{p}_n + \hat{t} - q_m; 0, \sigma_m)}{2\sigma_m^2 \sum_{n \in \mathcal{N}_Q(q_m)} \mathcal{N}(\hat{s}\hat{R}\hat{p}_n + \hat{t} - q_m; 0, \sigma_m)} \quad (11)$$

where the hatted quantities \hat{s} , \hat{R} , \hat{t} , and \hat{p}_n (\hat{p}_n as a result of \hat{c}) are the estimates from the last step and do not participate in the current optimization. EM yields an intuitive formulation, which rather than one hard correspondence, considers Q likely correspondences weighted by their probabilities computed from the last-step estimates. This increases the field of view of the model-measurement association step and can help move out of local minima. Both the pose and shape steps can use (10). Fig. 5 visualizes of the soft associations for $Q = 3$.

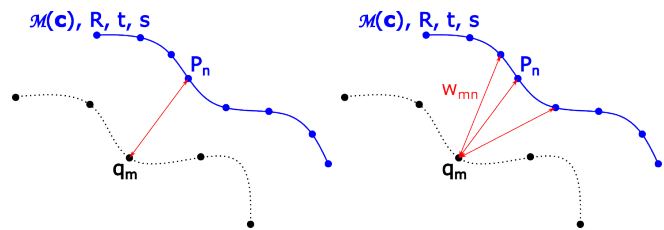


Fig. 5: Visualization of the original hard one-to-one association (left) and the EM soft associations for $Q = 3$ (right). $\mathcal{M}(c)$ is the ASM model that returns a mesh.

Multi-hypothesis estimation. Initialization is critical in avoiding local minima. The translation can be initialized as

the centroid of the observed point cloud $\bar{q} = \frac{1}{M} \sum_m q_m$. We find it better to begin with a small initial scale such as the average distance to the center $\frac{1}{M} \sum_m q_m - \bar{q}$. Without any neural network, the shape code is initialized to be the mean code for the category $\bar{c} = \frac{1}{U} \sum_u \tilde{c}_u$ where U is the total number of database object models for the category. However, rotation initial guess is not easily available. We thus track multiple initial rotation hypotheses in parallel and drop unpromising hypotheses quickly to save computation. Specifically, we start with the base $SO(3)$ grid from [53] as also used by [8]. The grid has 2304 discrete rotations uniformly covering $SO(3)$. During the course of optimization, we drop hypotheses according to the following three score functions:

Objective function. The mean residual in (7) $\mathcal{S}_r = \frac{1}{M} \sum_m r_m = \frac{1}{M} \sum_m \min_n \|\hat{s}\hat{R}\hat{p}_n + \hat{t} - q_m\|_2^2$ plus the standard deviation of it $\mathcal{S}_\sigma = \text{std}(\{r_m\}_{m=1}^M)$ is used. We find the addition of the standard deviation improves the results as we hope to have relatively uniform residuals over all the depth points.

Symmetry check. Man-made objects often have mirror symmetry (e.g. laptop and bowl) and rotation symmetry (e.g. bottle and can). If the estimated pose and shape are correct, mirroring and rotating the observed point cloud with respect to the estimated plane and axis of symmetry should still result in low residual. Let $\hat{T} = [\hat{s}\hat{R}\hat{t}; 0\ 0\ 0\ 1]$ be the $SIM(3)$ pose estimate, and $\hat{p}_{h,n} = [\hat{p}_n; 1]$ and $q_{h,m} = [q_m; 1]$ be the homogeneous coordinates of \hat{p}_n and q_m . The symmetry score $\mathcal{S}_{\psi,r}$ is

$$\frac{1}{M} \sum_m r_{\psi,m} = \frac{1}{M} \sum_m \min_n \|\hat{T}\hat{p}_{h,n} - \hat{T}T_\psi\hat{T}^{-1}q_{h,m}\|_2^2 \quad (12)$$

where $T_\psi = [R_\psi\ 0; 0\ 0\ 0\ 1]$ is a symmetry operation such as rotation around the axis of symmetry or reflection with respect to the plane of symmetry (in which case $\det(R_\psi) = -1$). (12) essentially transforms the observed point cloud to the object canonical pose using the current estimate \hat{T} , applies R_ψ , and transforms back so that the order of magnitude of $\mathcal{S}_{\psi,r}$ is similar to \mathcal{S}_r . The standard deviation score is $\mathcal{S}_{\psi,\sigma} = \text{std}(\{r_{\psi,m}\}_{m=1}^M)$ and the total symmetry score is $\mathcal{S}_\Psi = \frac{1}{\Psi} \sum_\psi \mathcal{S}_{\psi,r} + \mathcal{S}_{\psi,\sigma}$ for a total of Ψ different symmetry operations (multiple rotation symmetry operations of different angles are possible).

Depth rendering. Taking advantage of the mesh-based representation, we render the current estimates to a depth image and compare with the observed depth image of the object (after applying the segmentation mask). The depth rendering score is

$$\mathcal{S}_{dr} = \frac{1}{|\Omega(D)|} \sum_{d \in \Omega(D)} [R(\hat{T}, \mathcal{M}(\hat{c}), K_c)_d - D_d]^2 \quad (13)$$

where D is the masked observed depth image, $d \in \Omega(D)$ indexes pixels in the image space, R is the renderer, $\mathcal{M}(\hat{c})$ is the mesh model built from \hat{c} , and K_c includes the known camera intrinsics and other camera parameters (such as image size). We use the renderer from [49] and assign

the same background value to the rendered image and the masked observed depth image. The depth rendering helps to identify over-sized model (which may still give low \mathcal{S}_r if a portion of it fits the measurements well) [54]. To avoid computation overflow, we start depth rendering after the number of hypotheses is low.

The total score to be minimized is $\mathcal{S}_{tot} = \mathcal{S}_r + \mathcal{S}_\sigma + \lambda_\Psi \mathcal{S}_\Psi + \lambda_{dr} \mathcal{S}_{dr}$ where λ 's are the weights. When picking top hypotheses, we greedily select the next hypothesis at least 20 degrees apart from the last chosen hypothesis to alleviate duplicated or very close hypotheses.

Shape classification. To better initialize the shape code c , we build a shape classification network whose input is a color-coded normal vector image of the segmented object and the output is the index of the closest database model u^* . We choose ResNet-50 [55] for the network. The normal vector image is computed from the observed depth image and converted from $x, y, z \in [0, 1]$ (assuming unit vector) to RGB values. Only the image patch that contains the object (i.e. 2D bounding box) is resized to a constant size and fed to the network. We find the ground-truth closest model by computing Chamfer distance (1) between the ground-truth shape and all the models in the database (ShapeNet [48]). The final initial guess is \tilde{c}_{u^*} for the shape code. Note that if a model in the database is not matched to any ground-truth shape, it does not appear as a class in the network output. Therefore, the number of classes is smaller than or equal to the number of ground-truth shapes.

E. Summary

The full estimation algorithm is given in Alg. 1.

IV. EXPERIMENTS

A. Experiment Setup

Implementation. We implement our ShapeICP method with PyTorch [56] and PyTorch3D [49]. For the segmented depth image of an object, we perform statistical outlier removal on the back-projected point cloud as in [10], [57]. Moreover, we discard object detections that have points fewer than a threshold. All the hyperparameter values are summarized in the appendix.

Datasets. ShapeNetCore [48] is used to compute the ASM for the six categories in the NOCS REAL data [32]. For each category, we exclude weird-looking shapes, which is similarly done in [10]. As our model does not train on any pose-annotated data, synthetic benchmarks are irrelevant. We thus evaluate our method on the NOCS REAL test set. For the shape classification network, we use the NOCS REAL train set for training.

Baselines. We benchmark our ShapeICP method against several interesting baselines. *NOCS* [32] is the seminal work in this research area. *Neural Analysis-by-Synthesis* [16] is an optimization-based method that is not learning-based and does not rely on image sequences or strong application-specific constraints (see Section II-A for more details). *Metric Scale* [18] is a rare case of adopting a mesh-based shape representation. *ASM-Net* [10] also uses ASM but it

Input: Back-projected depth points of the object $\{q_m\}_{m=1}^M$; background-masked depth image D ; initial guesses \hat{t} , \hat{s} , and \hat{c} ; a set of G rotation guesses $\{\hat{R}_g\}_{g=1}^G$; an ASM with bases $\{b_k\}_{k=1}^K$; a set of symmetry operations $\{T_\psi\}_{\psi=1}^\Psi$

Output: Estimates of object pose and shape code \hat{R} , \hat{t} , \hat{s} , \hat{c} $\{\hat{t}_g, \hat{s}_g, \hat{c}_g\} \leftarrow \{\hat{t}, \hat{s}, \hat{c}\} \forall g$;

```

for iter = 1, 2, ..., maxIterations do
  if down-select hypotheses then
    for g = 1, ..., G do
      /* execute in parallel */
       $S_{tot,g} =$ 
       $S_{tot}(\hat{R}_g, \hat{t}_g, \hat{s}_g, \hat{c}_g; \{q_m\}_{m=1}^M, D, \{T_\psi\}_{\psi=1}^\Psi)$ ;
    end
    sort( $\{\hat{R}_g, \hat{t}_g, \hat{s}_g, \hat{c}_g\}_{g=1}^G$ ) by  $\{S_{tot,g}\}_{g=1}^G$ ;
    pick top hypotheses  $\{\hat{R}_g, \hat{t}_g, \hat{s}_g, \hat{c}_g\}_{g=1}^{G_{new}}$ ;
     $G \leftarrow G_{new}$ ;
  end
  for g = 1, ..., G do
    /* execute in parallel */
    Find the Q closest points  $\mathcal{N}_Q(q_m) \forall q_m$ 
     $\{\hat{R}_g, \hat{t}_g, \hat{s}_g\} \leftarrow$  solve (10) by Umeyama;
    if stop shape estimation then
      continue;
    end
    for step = 1, 2, ..., maxSteps do
      Find the Q closest points  $\mathcal{N}_Q(q_m) \forall q_m$ 
       $\hat{c}_g \leftarrow$  minimize  $\mathcal{L}_{sc}$  by one-step SGD;
      /* (10) instead of (7) in  $\mathcal{L}_{sc}$  */
    end
  end
end
return  $\{\hat{R}_{g=1}, \hat{t}_{g=1}, \hat{s}_{g=1}, \hat{c}_{g=1}\}$ 

```

Algorithm 1: ShapeICP

is point-based. Unlike our method, its inference is mainly performed by neural network regression. *Shape Prior* [1] also estimates the shape by deforming a prior but the method is learning-based. *CenterSnap* [34] is a one-shot end-to-end learning-based solution which is the opposite to our work.

Evaluation protocol and metrics. We use the public original NOCS evaluation code for the pose evaluation as done in most of the prior work. A small bug in the NOCS code was reported by [13]. We provide the updated results with the bug fixed in the appendix. For the shape evaluation, we use the Chamfer distance as the metric and follow the evaluation code from [1]. All the pose accuracy metrics in Table I and III are in terms of the percentage of the results that fall under the specified thresholds. IoU is the 3D overlap between the estimated 3D bounding box and the ground-truth 3D bounding box of the object. Most neural methods directly predict three scales along the three axes (x, y, z) for more accurate 3D bounding box prediction. To build the 3D bounding box, our method multiplies the estimated scale by the aspect ratios along the three axes of the estimated shape whose diagonal is normalized to unity.

B. Results

Table I shows the benchmarking results on NOCS REAL. Our method achieves overall surpassing or comparable performance to many data-driven approaches. As an

optimization-based approach, our method can reach very high accuracy once it finds the convergence basin around the ground-truth, which is evidenced by its dominating performance in the $5^\circ 5\text{cm}$ and $5^\circ 10\text{cm}$ metrics. The inability of our method to estimate three scales along the three axes is potentially the cause of the low IoU50 metric.

We particularly emphasize the comparison between our method and ASM-Net [10] since we both adopt ASM as the shape representation. Despite not using any pose-annotated data, our method surpasses ASM-Net, which fully leverages all the annotated data, by a significant margin. Our no-learning variation (w/o S.C.) is even stronger than their ICP-assisted version in the $5^\circ 5\text{cm}$ metric and closely comparable in the IoU75 and $10^\circ 5\text{cm}$ metrics. Moreover, we attain a distant win against the previous no-learning method, Neural Synthesis-by-Analysis [16], and the previous mesh-based method [18].

In Table II, we show the shape estimation results. Our method provides moderate performance overall, sitting in the middle among several learning-based methods. ASM-Net reaches better Chamfer distance than ours. The point-based ASM used by ASM-Net is more flexible (due to the undefined connectivity between points) than our mesh-based ASM though it is less expressive in the geometry (due to the loss of surface). The main limitation for our mesh-based ASM comes from the necessary template deformation step which restricts the mesh topology to the template topology, bringing in another source of error other than the error from the latent shape reconstruction. However, this limitation can be alleviated by manually engineering category-specific templates instead of a spherical template throughout. Additionally, our shape initialization network is a classification network not a regression network. It has the advantage of being failure-safe since even if it predicts something completely off, the prediction will still be a valid shape in the category, which is often less catastrophic than a really wrong prediction from a regression network. However, the failure-safe characteristic comes at the expense of losing the ability to interpolate or extrapolate, which results in lower accuracy.

In Fig. 6, we visualize some example results. The estimated objects in general fit the depth measurements very well, showing the effectiveness of our ShapeICP algorithm in minimizing the objective function (7). The error mostly stems from the inherent ambiguity in the problem, which manifests as local minima in the objective function landscape. We hypothesize that there may be even cases where the ground-truth is not the global minimum or is only one of the almost equal local minima. For example, a thin or a thick laptop may fit equally well to a front view of the laptop whose thickness is not observed. Our method notably tends to making mistakes on mugs and cameras as seen in Fig. 6. The orientation of these two categories of objects mostly depends on single local features such as the mug handle and the camera lens barrel. Because of this, the global minimum for the orientation has a very small convergence basin. Due to the unknown pose compounded with the unknown measurement-

TABLE I: Benchmarking results on NOCS REAL [32]. Baseline results are from sources [10], [35]. S.D. stands for shape-annotated data required for training and P.D. stands for pose-annotated data required for training. S.C. stands for the shape classification network. The results are roughly in the order of overall performance. The best result in each metric is in bold.

Method	P.D.	S.D.	IoU25	IoU50	IoU75	5°5cm	5°10cm	10°5cm	10°10cm
NOCS [32]	✓	✓	84.8	78.0	30.1	10.0	9.8	25.2	25.8
Synthesis [16]			–	–	–	0.9	1.4	2.4	5.5
Metric Scale [18]	✓	✓	81.6	68.1	–	5.3	5.5	24.7	26.5
ASM-Net w/o ICP [10]	✓	✓	–	64.4	31.7	12.4	–	37.7	–
ShapeICP(Ours) w/o S.C.			82.6	58.3	37.1	32.3	33.1	42.2	43.4
ASM-Net w/ ICP [10]	✓	✓	–	68.3	37.4	25.6	–	43.7	–
ShapeICP(Ours) w/ S.C.			82.1	58.0	42.2	36.5	37.1	50.6	51.4
ShapePrior [1]	✓	✓	81.2	77.3	53.2	21.4	21.4	54.1	54.1
CenterSnap [34]	✓	✓	83.5	80.2	–	27.2	29.2	58.8	64.4

TABLE II: Shape estimation results on NOCS REAL [32] evaluated with Chamfer distance (10^{-3}). Baseline results are from sources [10], [35]. S.D. stands for shape-annotated data required for training and P.D. stands for pose-annotated data required for training. S.C. stands for the shape classification network. The results are roughly in the order of overall performance.

Method	P.D.	S.D.	Bottle	Bowl	Camera	Can	Laptop	Mug	Mean
ShapePrior [1]	✓	✓	5.0	1.2	9.9	2.4	7.1	0.97	4.4
ShapeICP(Ours) w/o S.C.			2.5	0.86	9.1	3.7	3.7	2.8	3.8
Reconstruction [1]	✓	✓	3.4	1.2	8.9	1.5	2.9	1.0	3.2
ShapeICP(Ours) w/ S.C.			2.8	0.58	6.8	1.1	1.2	3.0	2.6
CenterSnap [34]	✓	✓	1.3	1.0	4.3	0.9	0.7	0.6	1.5
ASM-Net [10]	✓	✓	0.23	0.06	0.61	0.15	0.60	0.10	0.29

TABLE III: Ablation results on NOCS REAL [32].

Ablated Module	IoU75	5°2cm	5°5cm	10°2cm	10°5cm
EM	-1.5	-2.2	-4.0	-0.4	+0.2
Symm. Check	-0.3	-0.5	-0.5	-0.4	-0.4
Rendering	-0.6	-2.5	-2.2	-0.5	+0.2

to-model correspondences, fitting to these local features and finding the convergence basin for these objects are extremely difficult. In general, our algorithm has a tendency to have the bulk of the object fit well but ignore the local details.

C. Ablation

We ablate the modules for local minimum alleviation introduced in Section III-D to show their effectiveness. The ablation results are given in Table III. The symmetry check provides uniform improvements across the metrics. The EM treatment and the depth rendering check lead to more notable improvements in the higher accuracy metrics such as the 5°5cm and 5°2cm metrics.

D. ShapeICP versus Learning-based Methods

As discussed in Section IV-B, one limitation of our method is that the large ambiguity inherently in the problem causes the ground-truth minimum to be buried among many equally good minima. This problem manifests itself in that the estimated pose and shape fit the depth measurements very well (i.e. achieving low objective function value) but are different from the ground-truth. In such cases, it is a limitation of the objective function not the algorithm (i.e. solver). Another limitation is when the convergence basin of the global minimum is too small (e.g. mugs and cameras), our method has a hard time to find the basin. We consider that these are the cases where neural networks are helpful since

learning-based methods essentially solve a mapping problem from the input data to the output prediction instead of an optimization problem. On the other hand, our optimization-based approach shines when it finds the convergence basin, it can achieve very high accuracy as seen from the 5°5cm and 5°10cm metrics in Table I. Furthermore, our method can be quickly deployed in any new environments without curating an object pose dataset for training.

In terms of runtime, the current algorithm without code optimization runs on an Nvidia TITAN RTX GPU at about 7 seconds per object instance, which can be inferior to most learning-based methods at inference time. The most significant slowdown is from the multi-hypothesis tracking. However, parallel computation can be leveraged to run multiple instances in parallel. The runtime may also be acceptable in an online setting if the algorithm is run only on a sparse set of key-frames for static objects.

V. CONCLUSION

We proposed the ShapeICP algorithm for category-level object pose and shape estimation from a single depth image. Our method implements a novel mesh-based active shape model (ASM) to represent categorical object shape. Remarkably the method does not require any pose-annotated data, unlike the vast majority of the methods in the field. ShapeICP achieves surpassing or on-par performance to many learning-based methods which rely on pose-annotated data. Future directions include how to better disambiguate the problem potentially by exploring RGB-image-based constraints and how to better initialize the algorithm closer to the convergence basin of a global minimum.

REFERENCES

- [1] M. Tian, M. H. Ang, and G. H. Lee, “Shape prior deformation for categorical 6D object pose and size estimation,” in *Computer Vision–*

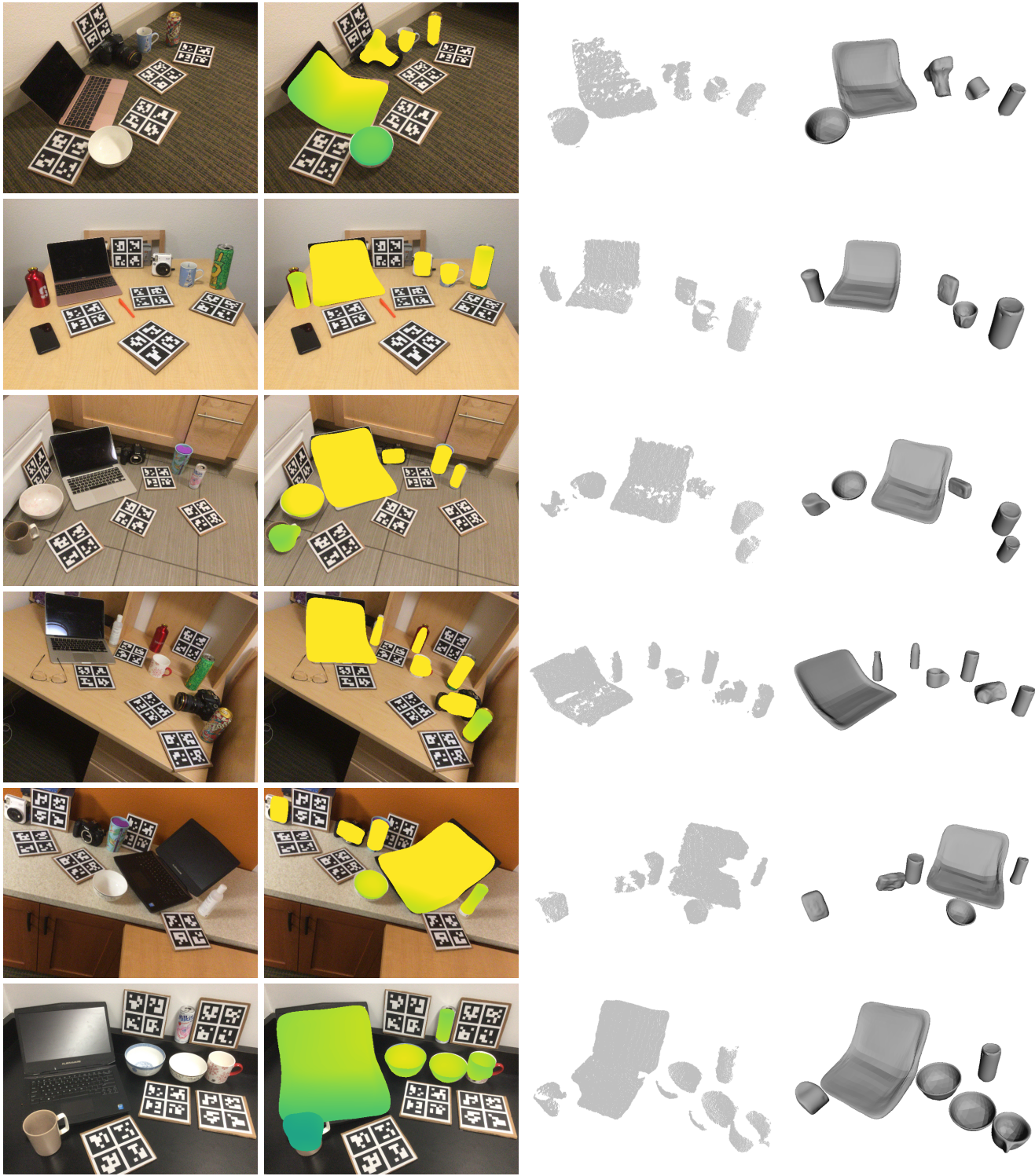


Fig. 6: Visualization of example NOCS REAL [32] frames. From left to right are the color image, the color image overlaid by the depth projection of the estimated objects, back-projected depth image, and estimated objects from a novel viewpoint.

ECCV 2020: 16th European Conference, Glasgow, UK, August 23–28, 2020, Proceedings, Part XXI 16. Springer, 2020, pp. 530–546.

- [2] K. Chen and Q. Dou, “SGPA: Structure-guided prior adaptation for category-level 6D object pose estimation,” in *Proceedings of the IEEE/CVF International Conference on Computer Vision*, 2021, pp. 2773–2782.
- [3] J. Wang, K. Chen, and Q. Dou, “Category-level 6D object pose estimation via cascaded relation and recurrent reconstruction networks,” in *2021 IEEE/RSJ International Conference on Intelligent Robots and Systems (IROS)*. IEEE, 2021, pp. 4807–4814.
- [4] R. Zhang, Y. Di, F. Manhardt, F. Tombari, and X. Ji, “SSP-Pose: Symmetry-aware shape prior deformation for direct category-level object pose estimation,” in *2022 IEEE/RSJ International Conference on Intelligent Robots and Systems (IROS)*. IEEE, 2022, pp. 7452–7459.
- [5] J. Lin, Z. Wei, C. Ding, and K. Jia, “Category-level 6D object

- pose and size estimation using self-supervised deep prior deformation networks,” in *European Conference on Computer Vision*. Springer, 2022, pp. 19–34.
- [6] R. Zhang, Y. Di, Z. Lou, F. Manhardt, F. Tombari, and X. Ji, “RBP-Pose: Residual bounding box projection for category-level pose estimation,” in *European Conference on Computer Vision*. Springer, 2022, pp. 655–672.
 - [7] D. Chen, J. Li, Z. Wang, and K. Xu, “Learning canonical shape space for category-level 6D object pose and size estimation,” in *Proceedings of the IEEE/CVF conference on computer vision and pattern recognition*, 2020, pp. 11 973–11 982.
 - [8] L. Bruns and P. Jensfelt, “SDFEst: Categorical pose and shape estimation of objects from RGB-D using signed distance fields,” *IEEE Robotics and Automation Letters*, vol. 7, no. 4, pp. 9597–9604, 2022.
 - [9] X. Deng, J. Geng, T. Bretl, Y. Xiang, and D. Fox, “iCaps: Iterative category-level object pose and shape estimation,” *IEEE Robotics and Automation Letters*, vol. 7, no. 2, pp. 1784–1791, 2022.
 - [10] S. Akizuki and M. Hashimoto, “ASM-Net: Category-level pose and shape estimation using parametric deformation,” in *BMVC*, 2021, p. 414.
 - [11] J. Lin, Z. Wei, Z. Li, S. Xu, K. Jia, and Y. Li, “DualPoseNet: Category-level 6D object pose and size estimation using dual pose network with refined learning of pose consistency,” in *Proceedings of the IEEE/CVF International Conference on Computer Vision*, 2021, pp. 3560–3569.
 - [12] S. Yu, D.-H. Zhai, Y. Guan, and Y. Xia, “Category-level 6-D object pose estimation with shape deformation for robotic grasp detection,” *IEEE Transactions on Neural Networks and Learning Systems*, 2023.
 - [13] H. Lin, Z. Liu, C. Cheang, Y. Fu, G. Guo, and X. Xue, “SAR-Net: Shape alignment and recovery network for category-level 6D object pose and size estimation,” in *Proceedings of the IEEE/CVF Conference on Computer Vision and Pattern Recognition*, 2022, pp. 6707–6717.
 - [14] J. Liu, W. Sun, C. Liu, H. Yang, X. Zhang, and A. Mian, “MH6D: Multi-hypothesis consistency learning for category-level 6-D object pose estimation,” *IEEE Transactions on Neural Networks and Learning Systems*, 2024.
 - [15] G. Li, Y. Li, Z. Ye, Q. Zhang, T. Kong, Z. Cui, and G. Zhang, “Generative category-level shape and pose estimation with semantic primitives,” in *Conference on Robot Learning*. PMLR, 2023, pp. 1390–1400.
 - [16] X. Chen, Z. Dong, J. Song, A. Geiger, and O. Hilliges, “Category level object pose estimation via neural analysis-by-synthesis,” in *Computer Vision—ECCV 2020: 16th European Conference, Glasgow, UK, August 23–28, 2020, Proceedings, Part XXVI 16*. Springer, 2020, pp. 139–156.
 - [17] R. Wang, N. Yang, J. Stueckler, and D. Cremers, “DirectShape: Direct photometric alignment of shape priors for visual vehicle pose and shape estimation,” in *2020 IEEE International Conference on Robotics and Automation (ICRA)*. IEEE, 2020, pp. 11 067–11 073.
 - [18] T. Lee, B.-U. Lee, M. Kim, and I. S. Kweon, “Category-level metric scale object shape and pose estimation,” *IEEE Robotics and Automation Letters*, vol. 6, no. 4, pp. 8575–8582, 2021.
 - [19] Y. Yoshitake, M. Nishimura, S. Nobuhara, and K. Nishino, “TransPoser: Transformer as an optimizer for joint object shape and pose estimation,” *arXiv preprint arXiv:2303.13477*, 2023.
 - [20] M. Shan, Q. Feng, Y.-Y. Jau, and N. Atanasov, “ELLIPSDF: Joint object pose and shape optimization with a bi-level ellipsoid and signed distance function description,” in *Proceedings of the IEEE/CVF International Conference on Computer Vision*, 2021, pp. 5946–5955.
 - [21] S. Umeyama, “Least-squares estimation of transformation parameters between two point patterns,” *IEEE Transactions on Pattern Analysis & Machine Intelligence*, vol. 13, no. 04, pp. 376–380, 1991.
 - [22] W. Wang, D. Ceylan, R. Mech, and U. Neumann, “3DN: 3D deformation network,” in *Proceedings of the IEEE/CVF Conference on Computer Vision and Pattern Recognition*, 2019, pp. 1038–1046.
 - [23] A. Badki, O. Gallo, J. Kautz, and P. Sen, “Meshlet priors for 3D mesh reconstruction,” in *Proceedings of the IEEE/CVF Conference on Computer Vision and Pattern Recognition*, 2020, pp. 2849–2858.
 - [24] R. Hanocka, G. Metzger, R. Giryes, and D. Cohen-Or, “Point2Mesh: A self-prior for deformable meshes,” *arXiv preprint arXiv:2005.11084*, 2020.
 - [25] J. Rock, T. Gupta, J. Thorsen, J. Gwak, D. Shin, and D. Hoiem, “Completing 3D object shape from one depth image,” in *Proceedings of the IEEE conference on computer vision and pattern recognition*, 2015, pp. 2484–2493.
 - [26] G. Gkioxari, J. Malik, and J. Johnson, “Mesh R-CNN,” in *Proceedings of the IEEE/CVF international conference on computer vision*, 2019, pp. 9785–9795.
 - [27] N. Wang, Y. Zhang, Z. Li, Y. Fu, W. Liu, and Y.-G. Jiang, “Pixel2Mesh: Generating 3D mesh models from single RGB images,” in *Proceedings of the European conference on computer vision (ECCV)*, 2018, pp. 52–67.
 - [28] T. F. Cootes, C. J. Taylor, D. H. Cooper, and J. Graham, “Active shape models—their training and application,” *Computer vision and image understanding*, vol. 61, no. 1, pp. 38–59, 1995.
 - [29] W. E. Lorensen and H. E. Cline, “Marching cubes: A high resolution 3D surface construction algorithm,” in *Seminal graphics: pioneering efforts that shaped the field*, 1998, pp. 347–353.
 - [30] P. J. Besl and N. D. McKay, “Method for registration of 3-D shapes,” in *Sensor fusion IV: control paradigms and data structures*, vol. 1611. Spie, 1992, pp. 586–606.
 - [31] A. Hornung, K. M. Wurm, M. Bennewitz, C. Stachniss, and W. Burgard, “OctoMap: An efficient probabilistic 3D mapping framework based on octrees,” *Autonomous robots*, vol. 34, pp. 189–206, 2013.
 - [32] H. Wang, S. Sridhar, J. Huang, J. Valentin, S. Song, and L. J. Guibas, “Normalized object coordinate space for category-level 6D object pose and size estimation,” in *Proceedings of the IEEE/CVF Conference on Computer Vision and Pattern Recognition*, 2019, pp. 2642–2651.
 - [33] D. P. Kingma and M. Welling, “Auto-encoding variational Bayes,” *arXiv preprint arXiv:1312.6114*, 2013.
 - [34] M. Z. Irshad, T. Kollar, M. Laskey, K. Stone, and Z. Kira, “Center-Snap: Single-shot multi-object 3D shape reconstruction and categorical 6D pose and size estimation,” in *2022 International Conference on Robotics and Automation (ICRA)*. IEEE, 2022, pp. 10 632–10 640.
 - [35] M. Z. Irshad, S. Zakharov, R. Ambrus, T. Kollar, Z. Kira, and A. Gaidon, “ShAPO: Implicit representations for multi-object shape, appearance, and pose optimization,” in *European Conference on Computer Vision*. Springer, 2022, pp. 275–292.
 - [36] A. O. Vuola, S. U. Akram, and J. Kannala, “Mask-RCNN and U-net ensembled for nuclei segmentation,” in *2019 IEEE 16th international symposium on biomedical imaging (ISBI 2019)*. IEEE, 2019, pp. 208–212.
 - [37] J. Redmon, S. Divvala, R. Girshick, and A. Farhadi, “You Only Look Once: Unified, real-time object detection,” in *Proceedings of the IEEE conference on computer vision and pattern recognition*, 2016, pp. 779–788.
 - [38] J. J. Park, P. Florence, J. Straub, R. Newcombe, and S. Lovegrove, “DeepSDF: Learning continuous signed distance functions for shape representation,” in *Proceedings of the IEEE/CVF conference on computer vision and pattern recognition*, 2019, pp. 165–174.
 - [39] H. Wang, Z. Fan, Z. Zhao, Z. Che, Z. Xu, D. Liu, F. Feng, Y. Huang, X. Qiao, and J. Tang, “DTF-Net: Category-level pose estimation and shape reconstruction via deformable template field,” in *Proceedings of the 31st ACM International Conference on Multimedia*, 2023, pp. 3676–3685.
 - [40] W. Chen, X. Jia, H. J. Chang, J. Duan, L. Shen, and A. Leonardis, “FS-Net: Fast shape-based network for category-level 6D object pose estimation with decoupled rotation mechanism,” in *Proceedings of the IEEE/CVF Conference on Computer Vision and Pattern Recognition*, 2021, pp. 1581–1590.
 - [41] J. Shi, H. Yang, and L. Carlone, “Optimal and robust category-level perception: Object pose and shape estimation from 2-D and 3-D semantic keypoints,” *IEEE Transactions on Robotics*, 2023.
 - [42] G. Pavlakos, X. Zhou, A. Chan, K. G. Derpanis, and K. Daniilidis, “6-DoF object pose from semantic keypoints,” in *2017 IEEE international conference on robotics and automation (ICRA)*. IEEE, 2017, pp. 2011–2018.
 - [43] A. Vaswani, N. Shazeer, N. Parmar, J. Uszkoreit, L. Jones, A. N. Gomez, Ł. Kaiser, and I. Polosukhin, “Attention is all you need,” *Advances in neural information processing systems*, vol. 30, 2017.
 - [44] A. Kundu, Y. Li, and J. M. Rehg, “3D-RCNN: Instance-level 3D object reconstruction via render-and-compare,” in *Proceedings of the IEEE conference on computer vision and pattern recognition*, 2018, pp. 3559–3568.
 - [45] M. Michalkiewicz, E. Belilovsky, M. Baktashmotlagh, and A. Eriksson, “A simple and scalable shape representation for 3D reconstruction,” *arXiv preprint arXiv:2005.04623*, 2020.
 - [46] V. Blanz and T. Vetter, “A morphable model for the synthesis of 3D faces,” in *Seminal Graphics Papers: Pushing the Boundaries, Volume 2*, 2023, pp. 157–164.

- [47] C. Cao, Y. Weng, S. Lin, and K. Zhou, "3D shape regression for real-time facial animation," *ACM Transactions on Graphics (TOG)*, vol. 32, no. 4, pp. 1–10, 2013.
- [48] A. X. Chang, T. Funkhouser, L. Guibas, P. Hanrahan, Q. Huang, Z. Li, S. Savarese, M. Savva, S. Song, H. Su *et al.*, "ShapeNet: An information-rich 3D model repository," *arXiv preprint arXiv:1512.03012*, 2015.
- [49] N. Ravi, J. Reizenstein, D. Novotny, T. Gordon, W.-Y. Lo, J. Johnson, and G. Gkioxari, "Accelerating 3D deep learning with PyTorch3D," *arXiv:2007.08501*, 2020.
- [50] H. Robbins and S. Monro, "A stochastic approximation method," *The annals of mathematical statistics*, pp. 400–407, 1951.
- [51] C. M. Bishop, "Pattern recognition and machine learning," *Springer google schola*, vol. 2, pp. 5–43, 2006.
- [52] S. A. Parkison, L. Gan, M. G. Jadidi, and R. M. Eustice, "Semantic iterative closest point through expectation-maximization." in *BMVC*, 2018, p. 280.
- [53] A. Yershova, S. Jain, S. M. Lavalley, and J. C. Mitchell, "Generating uniform incremental grids on SO(3) using the Hopf fibration," *The International journal of robotics research*, vol. 29, no. 7, pp. 801–812, 2010.
- [54] J. Wang, M. Rünz, and L. Agapito, "DSP-SLAM: Object oriented SLAM with deep shape priors," in *2021 International Conference on 3D Vision (3DV)*. IEEE, 2021, pp. 1362–1371.
- [55] K. He, X. Zhang, S. Ren, and J. Sun, "Deep residual learning for image recognition," in *Proceedings of the IEEE conference on computer vision and pattern recognition*, 2016, pp. 770–778.
- [56] A. Paszke, S. Gross, F. Massa, A. Lerer, J. Bradbury, G. Chanan, T. Killeen, Z. Lin, N. Gimeshein, L. Antiga *et al.*, "PyTorch: An imperative style, high-performance deep learning library," *Advances in neural information processing systems*, vol. 32, 2019.
- [57] F. Manhardt, G. Wang, B. Busam, M. Nickel, S. Meier, L. Minciullo, X. Ji, and N. Navab, "CPS++: Improving class-level 6D pose and shape estimation from monocular images with self-supervised learning," *arXiv preprint arXiv:2003.05848*, 2020.

DERIVATION OF EM

We start off by explaining the probability models (8)(9). Since our sensor is a depth camera, the correct association for a depth measurement at a pixel should be made by ray casting instead of looking for the closest point to q_m . Therefore, ideally $\mathcal{N}_Q(q_m)$ in (8) should find the Q closest points near the point of the first hit of the cast ray (Q points instead of one to account for association uncertainties caused by the errors in the object pose and shape). However, the approximation of the Euclidean closest points near q_m greatly simplifies the computation and has shown robustness in ICP. Likewise, (9) is also an approximation to simplify the computation. When the association is given for a pixel in a depth image, the uncertainty should only be along the ray through the camera optical center, the pixel, and the associated point (1D uncertainty). By using the 3D Gaussian approximation as in (9), we are assuming the sensor is not a depth camera but rather the following generative process that directly makes the spatial measurement:

$$q_m = sRp_{z_m} + t + \epsilon_m \quad (14)$$

where ϵ is Gaussian noise following $\mathcal{N}(0, \Sigma_m)$.

The independence assumption $q_m|z_m \perp z_{m'}$ (i.e. $\mathcal{P}(q_m|z_m, z_{m'}) = \mathcal{P}(q_m|z_m)$) is reasonable. If the measurement association is already given, the association of another measurement should provide no extra information. Similarly, $q_m|z_m \perp q_{m'}|z_{m'}$ is also reasonable. Given the associations, two measurements are assumed to be independent (unless there is some systematic bias of the sensor). The assumption of all the latent variables (z_m 's) being independent of each other is not totally valid for a depth camera because the association at one pixel gives away the ray orientation (i.e. the bearing of the camera along that ray) and the association of the next pixel can only be made on a cone with its center line being the ray given by the first association. Nevertheless, for the generative model (14), it is reasonable to assume that the association of one measurement does not provide information to another association (z_m 's are independent of each other. i.e. $z_m \perp z_{m'}$) and it also greatly simplifies the derivation of EM.

To derive EM, we begin with the data likelihood:

$$\begin{aligned} \mathcal{P}(q_m) &= \sum_n \mathcal{P}(q_m|z_m = n)\mathcal{P}(z_m = n) \\ &= \sum_{n \in \mathcal{N}_Q(q_m)} \frac{1}{Q} \mathcal{N}(sRp_n + t - q_m; 0, \Sigma_m) \end{aligned} \quad (15)$$

Making use of the independence assumptions and denoting

$$\mathcal{Z} = \{z_m\}_{m=1}^M,$$

$$\begin{aligned} \mathcal{P}(\{q_m\}_{m=1}^M|\mathcal{Z}) &= \prod_{m=1}^M \mathcal{P}(q_m|\mathcal{Z}) \\ &= \prod_{m=1}^M \mathcal{P}(q_m|z_m) \\ &= \prod_{m=1}^M \mathcal{N}(sRp_{z_m} + t - q_m; 0, \Sigma_m) \end{aligned} \quad (16)$$

where the first equality assumes $\mathcal{P}(q_m|z_m) \perp \mathcal{P}(q_{m'}|z_{m'})$ and the second equality assumes $\mathcal{P}(q_m|z_m, z_{m'}) = \mathcal{P}(q_m|z_m)$. Since we have further assumed all the latent variables (z_m 's) are independent of each other, it leads to

$$\mathcal{P}(\mathcal{Z}) = \begin{cases} \frac{1}{Q^M} & \text{if } z_m \in \mathcal{N}_Q(q_m) \forall m \\ 0 & \text{otherwise} \end{cases} \quad (17)$$

We can now compute the posterior probability of the latent variables:

$$\begin{aligned} \mathcal{P}(\mathcal{Z}|\{q_m\}_{m=1}^M) &= \frac{\mathcal{P}(\mathcal{Z}, \{q_m\}_{m=1}^M)}{\mathcal{P}(\{q_m\}_{m=1}^M)} \\ &= \frac{\mathcal{P}(\{q_m\}_{m=1}^M|\mathcal{Z})\mathcal{P}(\mathcal{Z})}{\sum_{\mathcal{Z}} \mathcal{P}(\{q_m\}_{m=1}^M|\mathcal{Z})\mathcal{P}(\mathcal{Z})} \end{aligned} \quad (18)$$

whose result is

$$\begin{cases} \frac{\frac{1}{Q^M} \prod_{m=1}^M \mathcal{N}(sRp_{z_m} + t - q_m; 0, \Sigma_m)}{\sum_{\mathcal{Z}} \frac{1}{Q^M} \prod_{m=1}^M \mathcal{N}(sRp_{z_m} + t - q_m; 0, \Sigma_m)} & \text{if } z_m \in \mathcal{N}_Q(q_m) \forall m \\ 0 & \text{otherwise} \end{cases} \quad (19)$$

In the expectation step, we need to compute $\sum_{\mathcal{Z}} \hat{\mathcal{P}}(\mathcal{Z}|\{q_m\}_{m=1}^M) \ln \mathcal{P}(\mathcal{Z}, \{q_m\}_{m=1}^M)$, where $\hat{\mathcal{P}}(\mathcal{Z}|\{q_m\}_{m=1}^M)$ is given a hat notation to indicate that it is computed from the last available estimates [51]:

$$\begin{aligned} \sum_{\mathcal{Z}} \hat{\mathcal{P}}(\mathcal{Z}|\{q_m\}_{m=1}^M) \ln \mathcal{P}(\mathcal{Z}, \{q_m\}_{m=1}^M) &= \frac{1}{\sum_{\mathcal{Z}} \frac{1}{Q^M} \prod_{m=1}^M \mathcal{N}(\hat{s}\hat{R}\hat{p}_{z_m} + \hat{t} - q_m; 0, \Sigma_m)} \\ &= \sum_{\mathcal{Z}} \left\{ \frac{1}{Q^M} \left[\prod_{m=1}^M \mathcal{N}(\hat{s}\hat{R}\hat{p}_{z_m} + \hat{t} - q_m; 0, \Sigma_m) \right] \right. \\ &\quad \left. \sum_{m=1}^M \ln \frac{1}{Q} + \ln \mathcal{N}(sRp_{z_m} + t - q_m; 0, \Sigma_m) \right\} \end{aligned} \quad (20)$$

where $\sum_{\mathcal{Z}}$ is over all possible combinations of $\{z_m \in \mathcal{N}_Q(q_m)\}_{m=1}^M$. To simplify (20), we examine the pattern in a simple case. Suppose we have three measurements ($M = 3$) and we use a, b, c to denote the three $\frac{1}{Q} \mathcal{N}(\hat{s}\hat{R}\hat{p}_{z_m} + \hat{t} - q_m; 0, \Sigma_m)$ terms. We then use a', b', c' to denote the three $\ln \frac{1}{Q} + \ln \mathcal{N}(sRp_{z_m} + t - q_m; 0, \Sigma_m)$ terms. Suppose for each measurement, we have two possible associations (i.e. 2 realizations of z_m and 8 realizations of \mathcal{Z} for 3 measurements) which are denoted by subscript 1 and 2. The normalization term $\sum_{\mathcal{Z}} \frac{1}{Q^M} \prod_{m=1}^M \mathcal{N}(\hat{s}\hat{R}\hat{p}_{z_m} + \hat{t} - q_m; 0, \Sigma_m)$

becomes

$$\begin{aligned} & a_1 b_1 c_1 + a_2 b_1 c_1 + a_1 b_2 c_1 + a_2 b_2 c_1 \\ & + a_1 b_1 c_2 + a_2 b_1 c_2 + a_1 b_2 c_2 + a_2 b_2 c_2 \end{aligned}$$

The remaining term becomes

$$\begin{aligned} & a_1 b_1 c_1 (a'_1 + b'_1 + c'_1) + a_2 b_1 c_1 (a'_2 + b'_1 + c'_1) \\ & + a_1 b_2 c_1 (a'_1 + b'_2 + c'_1) + a_2 b_2 c_1 (a'_2 + b'_2 + c'_1) \\ & + a_1 b_1 c_2 (a'_1 + b'_1 + c'_2) + a_2 b_1 c_2 (a'_2 + b'_1 + c'_2) \\ & + a_1 b_2 c_2 (a'_1 + b'_2 + c'_2) + a_2 b_2 c_2 (a'_2 + b'_2 + c'_2) \end{aligned}$$

If we look at the coefficient of a'_1 , it is $a_1(b_1 c_1 + b_2 c_1 + b_1 c_2 + b_2 c_2)$ which is cancelled with the normalization term to only leave $\frac{a_1}{a_1 + a_2}$. Similarly, the coefficient of a'_2 is $\frac{a_2}{a_1 + a_2}$, the coefficient of b'_2 is $\frac{b_2}{b_1 + b_2}$ and so forth. If we gather the terms, (20) in this simple case is simplified to

$$\begin{aligned} & \frac{a_1 a'_1}{a_1 + a_2} + \frac{a_2 a'_2}{a_1 + a_2} + \frac{b_1 b'_1}{b_1 + b_2} \\ & + \frac{b_2 b'_2}{b_1 + b_2} + \frac{c_1 c'_1}{c_1 + c_2} + \frac{c_2 c'_2}{c_1 + c_2} \\ & = \frac{a_1 a'_1 + a_2 a'_2}{a_1 + a_2} + \frac{b_1 b'_1 + b_2 b'_2}{b_1 + b_2} + \frac{c_1 c'_1 + c_2 c'_2}{c_1 + c_2} \end{aligned}$$

We recognize that there is an outer summation over the measurements (one term each for a , b , and c), and for each measurement term in the summation, both the denominator and the numerator are summations over the associations (realizations of z_m indicated by subscripts 1 and 2). With this pattern, (20) in general is simplified to

$$\begin{aligned} & \sum_{m=1}^M \left\{ \frac{1}{\sum_{z_m \in \mathcal{N}_Q(q_m)} \frac{1}{Q} \mathbf{N}(\hat{s} \hat{R} \hat{p}_{z_m} + \hat{t} - q_m; 0, \Sigma_m)} \right. \\ & \quad \left. \sum_{z_m \in \mathcal{N}_Q(q_m)} \left[\frac{1}{Q} \mathbf{N}(\hat{s} \hat{R} \hat{p}_{z_m} + \hat{t} - q_m; 0, \Sigma_m) \right. \right. \\ & \quad \left. \left. \left(\ln \frac{1}{Q} + \ln \mathbf{N}(s R p_{z_m} + t - q_m; 0, \Sigma_m) \right) \right] \right\} \quad (21) \end{aligned}$$

Assuming isotropic covariance $\Sigma_m = \text{diag}(\sigma_m^2)$ and considering only the terms that involve $s R p_{z_m} + t$ (other terms are irrelevant in maximization), we obtain (10) by maximizing (21).

IMPLEMENTATION DETAILS

We present all the parameter settings in our algorithm in Table IV.

TABLE IV: Algorithm hyper-parameters

Description	Value
Number of neighbors in outlier removal	500
Number of standard deviations in outlier removal	1
Number of points threshold to ignore a detection	100
Number of vertices in the mesh template	2562
Number of points sampled in template deformation (Section III-B $N = M$)	5000
λ_n	0.01
λ_e	1.0, 3.0 (mug), 5.0 (camera)
λ_l	0.1, 0.01 (mug), 0.3 (can)
SGD learning rate	1.0
SGD momentum	0.9
Number of PCA components ¹	8, 50, 40, 5, 32, 7
Number of pose steps per iteration	1
Number of shape gradient descent steps per iteration	5
Total number of iterations for shape	50
Total number of iterations for pose	80
Number of points sampled on the mesh during estimation	1000
EM Q	5
EM σ^2	0.2
Mirror Symmetry Objects	all six NOCS objects ²
Rotation Symmetry Objects	bottle, bowl, mug ³ , can
Number of discrete rotation symmetry	6
Depth rendering start iteration ⁴	5
λ_Ψ	1.0
λ_{dr}	1.0
Depth rendering background value (units follow NOCS depth images)	5×10^3
Down-selection iteration	1, 5, 15
Number of hypotheses kept	2304 (initially), 45, 15, 1
Down-selection rotation spacing	20°

¹ in the order of bottle, bowl, camera, can, laptop, and mug. ² Camera is treated as mirror symmetric.

³ Mug is treated as rotation symmetric. ⁴ to reduce computation.